Lifetime Prediction of Actuation Fatigue in Shape Memory Alloy Notched Members

A Thesis

Presented to

the Faculty of the Department of Mechanical Engineering

University of Houston

In Partial Fulfillment

of the Requirements for the Degree

Bachelor of Science

in Mechanical Engineering

by

Rutvik Mehta

December 2018

Lifetime Predictions of Actuation Fatigue for Shape Memory Alloy Notched Members

Rutvik Mehta

Approved:

Chair of the Committee
Dr. Theocharis Baxevanis, Assistant Professor,
Mechanical Engineering

Committee Members:

Committee Member
Dr. Jagannatha Rao, Associate Professor and Chair,
Mechanical Engineering

Committee Member
Dr. Anastassios Mavrokefalos, Assistant Professor,
Mechanical Engineering

Dr. Suresh K. Khator, Associate Dean,
Cullen College of Engineering

Dr. Pradeep Sharma, Professor and Chair,
Mechanical Engineering

Acknowledgements

The first acknowlegement is to the Creator for providing me with great oppurtunities in life and giving me the motivation and courage to carry on during times of struggle. I would like to thank my parents for all the loving support they have provided and giving me the motivation necessary to keep moving forward. I would like to acknowledge Dr. Theocharis Baxevanis for giving the oppurtunity to do research with him and his team. His patience, guidance, advice and teachings throughout the thesis are greatly appreciated. Lastly, I would like to acknowledge M.d. Mehedi Hasan for answering the questions I had and thank all my peers who helped me during the thesis.

Lifetime Predictions of Actuation Fatigue in Shape Memory Alloy Notched Members

An Abstract

Presented to

the Faculty of the Department of Mechanical Engineering

University of Houston

In Partial Fulfillment

of the Requirements for the Degree

Bachelor of Science

in Mechanical Engineering

by

Rutvik Mehta

December 2018

Abstract

Shape Memory Alloy (SMA)-based solid state actuators are an attractive alternative to conventional actuators when a small volume and/or large force and stroke are required. These alloys have the unique characteristic of being able to accommodate large recoverable strains through repeated martensitic-austenitic phase transformation. Insufficient understanding of the SMA "actuation" fatigue properties and lack of theoretical models for accurate prediction of fatigue life are the main limiters for their wider acceptance in engineering applications. The efficiency of the Smith–Watson–Topper model combined with the field intensity approach in estimating fatigue life for loaded notched SMA members undergoing thermal cycling is demonstrated. The field intensity approach adopted, which characterizes damage over a critical region where failure mechanisms are highly active rather than at a single point, is more reasonable from the point of view of fatigue failure mechanisms and more comprehensive from the point of view of explaining fatigue phenomena.

Table of Contents

List of Figures

List of Tables

1 Introduction

Shape Memory Alloys (SMA) are a revolutionary material that possess properties that conventional materials lack. An SMA is an alloy, composed of two or more elements, which can regain its original shape prior to the deformation by reverse phase transformation from martensite to austenite caused by an external thermomechanical stimuli [2, 3]. This phenomenon presents two remarkable properties called pseudoelasticity (superelasticity) and the shape memory effect (SME). The first property is witnessed when an SMA transforms from austenite to martensite upon mechanical loading and upon unloading transforms back to the austenitic phase. The SME, on the other hand, is what allows for the actuation to take place. SMAs experience the SME when undergoing transformation induced by temperature variance while under constant stress. The resulting energy released during phase transformation is actuation energy.

The above properties allow for integration in various everyday applications leading to demand in numerous industrial areas such as manufacturing, aerospace, automotive, healthcare etc. One such application is SMA actuators. SMA based solid state actuators ensure a mechanical response with temperature changes by the means of heating or an electrical current. As a result, they are believed to be a potential alternative to traditional electromagnetic actuators in applications where a small volume or large actuation force is required [4, 5, 6]. This adaptation allows for simplified designs and lightweight and compact components which improves performance and reliability while reducing costs [7]. During actuation, however, the SMA undergoes phase transformation which leads to some irrecoverable strain, known as Transformation Induced Plasticity (TRIP) [8]. As a result, with repeated actuation, the material deteriorates leading to a finite lifetime which needs to be known for successful operation. This behavior is termed as actuation fatigue.

To successfully implement SMA actuators into applications, it is imperative to understand their deformation and failure response. Many industries have an agency that regulate the safety of new materials. For example, the FAA is responsibe for the aerospace industry and the FDA for the biomedical industry which have strict requirements on the safe operation of actuators and fatigue performance respectively [9]. As a result, it is necessary to find a predictive model capable of predicting failure response. The predictive fatigue models are considered to predict the lifetime of SMAs so that they can be used in design and optimization.

Primarily there are two dominant categories for fatigue models: life based and damage tolerant. Life based fatigue models are for situations where up to 90% of the fatigue life is spent towards crack initiation [10, 11]. As a result, they work best for situations where crack propogation do not have a large impact on the fatigue life. These would be for specimens or materials that would experience failure shortly after crack initiation. These models are widely used when designing against fatigue crack initiation. On the other hand, the damage tolerant models are a fracture mechanics approach to fatigue design. The basic premise is that all engineering components are inherently flawed [10]. In this category, the specimen is subjected to stresses *higher* than prescribed after the largest crack is detected using various techniques. These models work best for stable crack growth life [12]. The useful fatigue life is then defined as the number of cycles to propogate the crack to a critical length [10].

The most well known damage model is the Paris Law. This law assumes that a crack pre-exists in a body and that it grows with each cycle. When the crack reaches a critical length, fracture occurs [13]. The specimens used, in this study, have a short life after crack initiation due to the thickness making this law infeasible. Further, in this thesis, the crack kinematics, or the crack propagates, is not of interest. As a result, the life based models are of interest and the two models that are considered are the Continuum Damage Models and Critical Plane Models.

The continuum damage models calculate the damage the specimen experiences with cycle by calculating a damage parameter. The critical plane models, on the other hand, are based on the premise that failure occurs due to a crack. The crack will form and run on a 'critical plane', which has the most favorable stress and/or strain conditions for crack propogation [14]. These models aim to be for specimens that will be experiencing large amounts of normal stress and strain. It assumes that fatigue life can be calculated from the damage accumulated at the critical plane of the crack initiation point [15]. Since locating where the crack initiation will occur is of interest, the best option would be the critical plane approach. The critical plane model has stress-based models and strain-based models. The stress-based models are used usually for high fatigue or low plasticity areas whereas strain-based models are for low-cycle fatigue. Since this model will be experiencing low-cycle fatigue, the strain-based models are chosen [15].

The objective of this thesis is to determine whether the chosen critical plane model, the SWT model, accurately predicts the lifetime of notched specimen. The center-hole and notched-hole geometries are used to validate this model. The geometries are constructed in the form of plate actuators which are simulated on Abaqus and the results are post-processed using a Python script to calculate the SWT parameters. The SWT parameters are plotted and an evolution equation is formulated for each point as a function of distance from the notch. This equation is combined with Palmgren-Miner's Law, a fractional damage model, to determine the lifetime of the specimens. This equation is used in the least-square fit with other experiments of the same geometry to calibrate parameters that would lead to an accurate lifetime prediction. The predicted lifetimes calculated using the calibrated equation will be compared to the experimental lifetime. By validation, a viable alternative for determining the fatigue life of specimens with stress concentrators will be available.

2 Literature Review

2.1 Phase Transformations and TRIP in Shape Memory Alloys

SMAs consist of 2 crystal structures, austenite and martensite [16]. Austenite is considered the parent phase due to its high symmetry and stability, whereas martensite is the phase that is formed when a transformation occurs due to an applied stress and/or thermal load. Martensite can be categorized into twinned and detwinned martensite or stress induced martensite (SIM). In the absence of stress, martensite has self-accommodating variants where the SMA tries to phase change in a way that reduces shape distortion leading to low strains. By applying an external load the variants start to reorient (detwin) themselves towards the direction of loading. The preferred martensitic variant leads to large strains in the SMA [1].

Figure 1 shows the transformation that can occur from austenite to each martensitic stage via temperature and applied stress. The transition from twinned to detwinned martensite occurs when the stress is above the 'detwinning start stress', σ_s, and will completely transform if the load applied corresponds at or above the 'detwinning finish stress', σ_f [1].

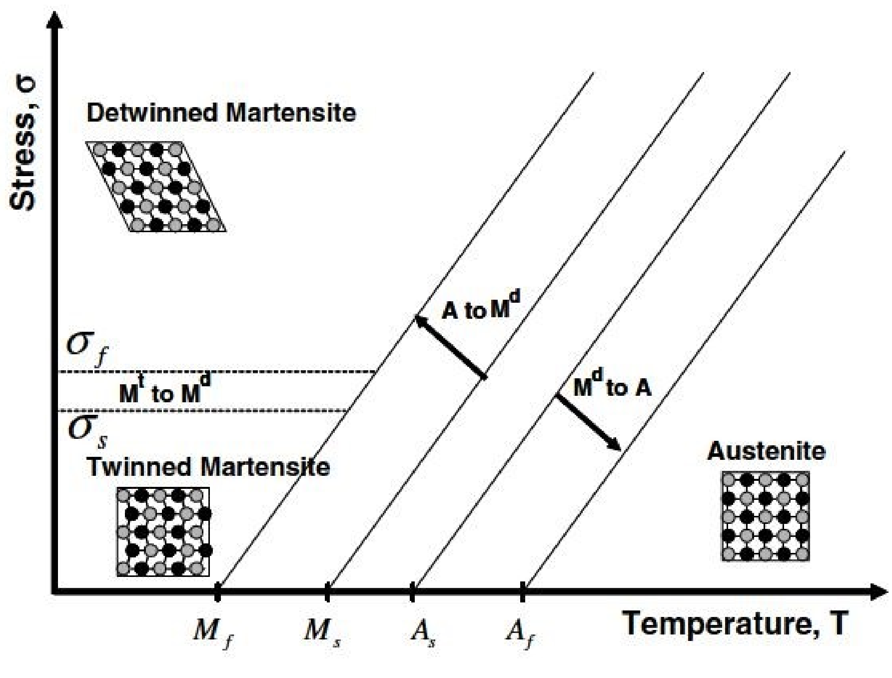

Figure 1: Stress-Temperature Phase Diagram [1]

The SME is associated with recovering the original shape of an SMA after a thermomechanical load [17]. By following the correct thermomechanical path, the SMA is able to recover both the elastic and transformation strain through phase transformation. The SME is initiated by applying a load when the SMA is in the twinned martensitic phase and then unloaded at a temperature below A_s and finally heating above A_f to recover the initial shape. Figure 2 illustrates this process in more detail during actuation. In this diagram, A to B shows the temperature decrease leading from austenite to twinned martensite. A load is then applied to the SMA specimen which leads to a transformation from twinned to detwinned martensite. The load is then removed at a temperature below A_s, as shown from C to D, and then heated above A_f from E to F to shape recovery [1]. This is most commonly called the 'One Way Memory Effect' (OWME). In addition, there is also a 'Two Way Memory Effect' (TWME), where the SMA goes directly from austenite to the detwinned martensitic phase during cooling under no load. This is not a native attribute of an SMA and can be acquired by doing SIM and SME cycles, called 'training' [18].

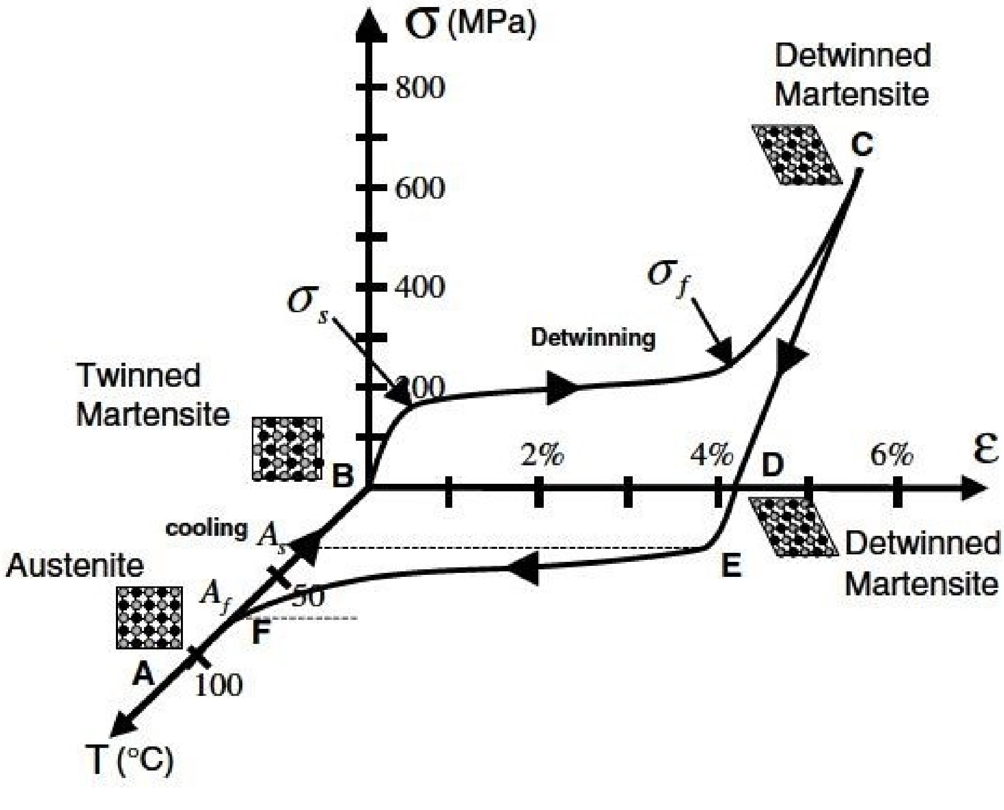

Figure 2: Stress-Strain-Temperature Phase Diagram showing Shape Memory Effect [1]

Pseudoelasticity shows the elasticity property of the material. Pseudoelasticity can be clearly seen when the SMA is at the austenitic phase and a large load is applied which starts the transformation. When the stresses on the SMA exceeds the critical stress, σ^{Ms}, martensitic transformation starts and upon reaching σ^{Mf}, austenite has fully transformed into martensite. The resultant martensite is detwinned since a large load has been applied. By removing the load, the SMA would revert back to austenite. Note that as the temperature increases, the stress required to initiate the start of phase transformation increases [19].

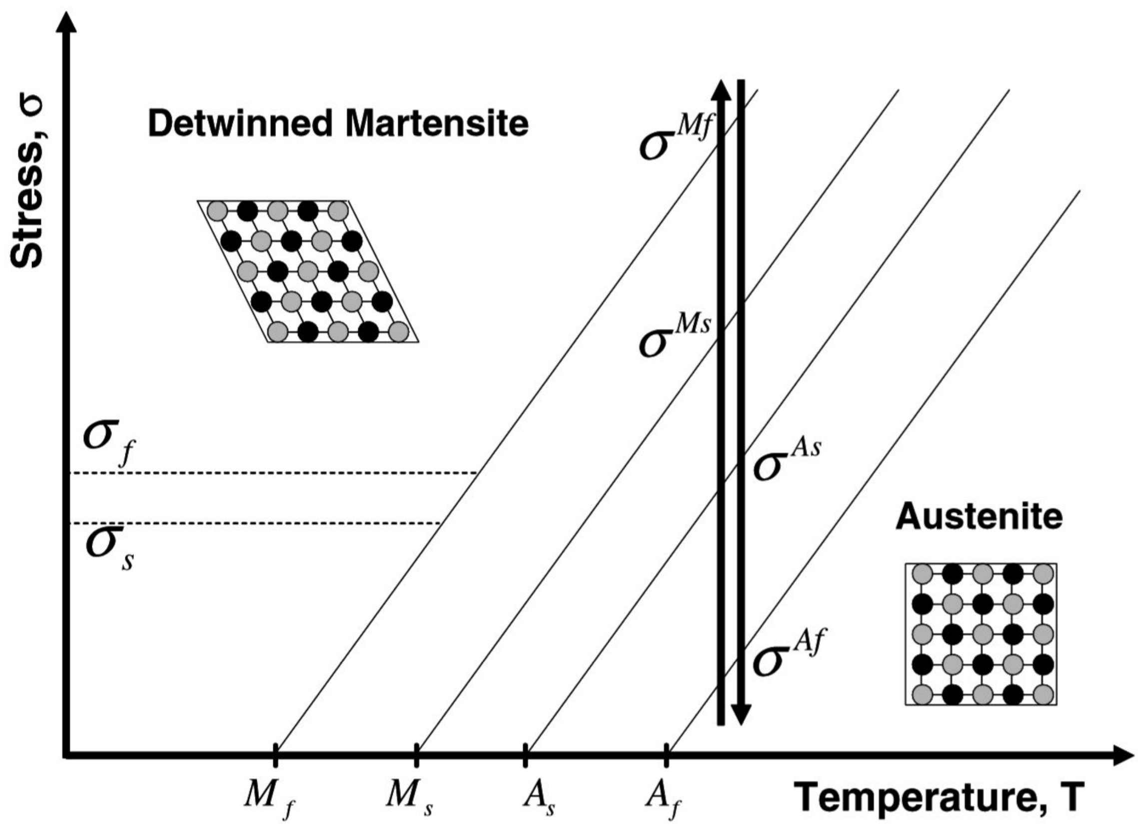

Figure 3: Pseudoelastic Loading Path

The difference between the two properties is that the SME is used during isobaric scenarios whereas, pseudoelasticity is during isothermal scenarios. Note that an SMA undergoing pseudoelasticity does have TRIP if stresses are exceeded more than σ^{Ms}, inducing phase transformation. During transformation, there are three types of strain, as shown in Eq. 1.

$$\varepsilon^T = \varepsilon + \varepsilon^t + \varepsilon^p, \tag{1}$$

where ε^T is the total strain, ε is the elastic strain, ε^t is the transformation strain, and ε^p is the plastic strain.

In Eq. 1, the elastic and transformation strain are both recoverable after each cycle while plastic strain is irrecoverable. Most SMAs can recover between 2 to 10 percent strain which reduces with increasing cycles [20]. During cycling, the irrecoverable strain causes permanent deformations originating from the transition layer, or habit plane, between austenite and martensite in an effort to accommodate the martensitic variants [1]. The stress that is produced at this plane is due to the misfit between the austenitic and martensitic phases which drive the dislocation activity resulting in permanent microstructural changes known as plastic strains [4]. This phenomenon results in plastic strain occurring at a stress below the plastic yield limit of the material [1].

TRIP is the largest during the initial cycles, since the local stresses exceed the theoretical shear stress, and diminishes with increasing cycles until stabilization as shown in Figure 4. This has been postulated because after the dislocations reach the grain boundaries they will be immobile. Isobaric experiments, however, have shown that the value never saturates until failure [1].

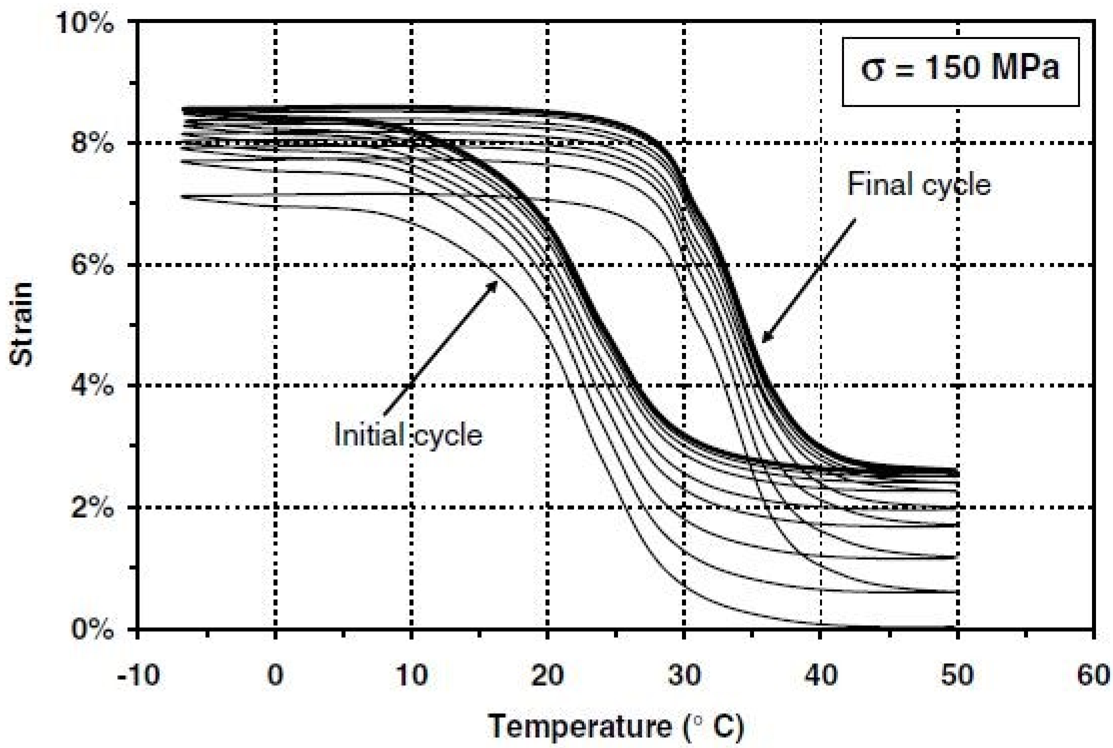

Figure 4: Temperature - Strain Graph under Constant Mechanical Load

2.2 Actuation Fatigue of SMA

SMAs experience two types of fatigue, mechanical and actuation fatigue. Mechanical fatigue is pseudoelastic cycling under constant temperature. This has been studied extensively and has a vast amount of literature available [21, 22, 23, 24, 25] . Actuation fatigue, or thermomechanical fatigue, are thermal cycles under a constant-stress loading condition and is still a developing area. The first actuation fatigue test was conducted by Bigeon and Morin in 1996 where SMA wires underwent complete transformation under a constant load until failure [26]. Repeated actuation causes an accumulation of dislocations which affects the functionality. This plastic strain, or TRIP, causes many changes to a specimen which directly affect its properties. All these properties are interconnected and occur due to dislocations. Firstly, the minimum critical stress required for the onset of martensitic transformation (σ^{Ms}) decreases because of the increasing presence of dislocations with cycle causing local stresses. These pre-existing stresses in that region help the material to transform before the stress reaches the previous cycle's critical stress for the onset of transformation. As the local stresses increase, with cycle, the onset for transformation decreases. Secondly, once the dislocations reach the grain boundaries more stress is required to achieve the same amount of strain as the previous cycle. This is termed transformation hardening. With each cycle, the hardening term increases. A visual representation can be seen on a stress-strain curve by noticing an increase in slope during the transformation of consecutive cycles. Lastly, the hysteresis loop decreases. The hysteresis loop shows the loading and unloading path for the specimen and the area that is enclosed within these paths show the dissipation energy. This area decreases with the number of cycles until stabilization.

2.3 Smith-Watson-Topper Model

To determine the number of cycles to failure, or fatigue life, a robust model is needed to determine the damage the material is experiencing with each cycle. There are a variety of critical plane models available, as discussed above, and among them the Smith-Watson-Topper (SWT) model was chosen. This model was developed in 1970 by K.N Smith, P. Watson, and T. H. Topper to develop a function that would be able to predict fatigue damage over loading cycles [27]. In the beginning, Bigeon and Morin and Scire Mammano and Dragoni developed the Wohler's S-N strength-life curves using experimental data [28, 29]. The power law, $\sigma = aN_f^{-b}$, correlates well with data, however, a flaw exists in the model which is that at least one of the parameters, a and/or b, need to be changed based on whether complete or partial phase transformation occurs for the same stress level [26, 30, 31]. The Manson-Coffin model was also used, however, the parameters vary for different stress values. Furthermore, both models have not been able to determine the plane where crack initiation will occur and on which plane it will propagate. It is, therefore, proposed that the SWT will be able to predict actuation fatigue lifetimes for a material system that undergoes full and partial transformation at stress levels using just two empirical parameters [26].

This model has been recognized by both researchers and engineers due to its success and accuracy in determining the fatigue life of conventional materials [32]. Past results have shown that the SWT has been successful for isobaric, uniaxial material systems [27] and that it works best with brittle materials [33]. Now, since SMAs fail predominantly in a brittle manner, this model was extended into SMA fatigue life calculations. Previous work done using this model have used simple geometries to calculate the lifetime [26].

The SWT works by taking into account the principle strain amplitude and the stress in the direction of the maximum principle strain as shown in Eq. 2 [27]. The output is a SWT parameter, known as a fatigue parameter which is calculated for each cycle. This parameter shows the amount of fatigue the material experiences.

$$\sigma_{max}\varepsilon_{\alpha} = aN_f^{-b}, \tag{2}$$

where N_f is the actuation lifetime and a and b are empirical parameters.

The variables, a and b, are found empirically through curve fitting of the uniaxial experimental results [20]. This model is based on the premise that the fatigue life is dominated by crack initiation and growth along tensile planes [27]. The SWT parameter can be taken as the actuation strain energy density [34] since the product of strain and stress gives the dimensions of energy. Previous work has demonstrated that the parameter is proportional to the energy dissipated during phase transformation, which was proven successful for the prediction of the purely mechanical fatigue of SMAs. In [26], it can be seen that the SWT was able to accurately predict the lifetimes of the

SMAs investigated for both partial and full transformation at different loadings. Figures 5 and 6 show the results for the SMA materials. One thing noted was that for complex actuation loading paths, a constitutive law is needed to determine the evolution of the SWT parameter with cycling.

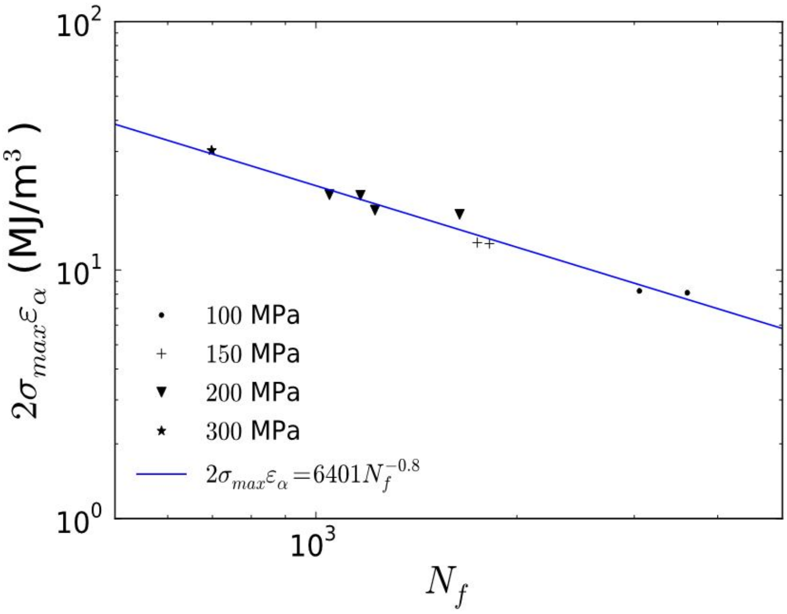

Figure 5: SWT Curve Fitting for $Ni_{50}Ti_{50}$

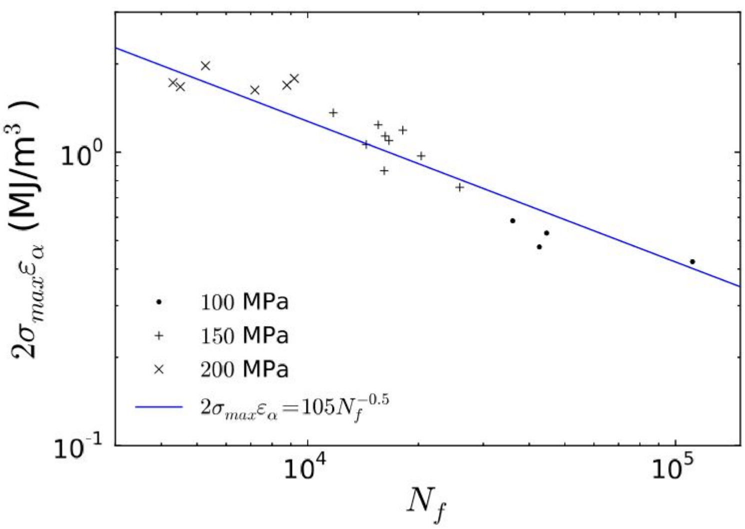

Figure 6: SWT Curve Fitting for $Ni_{60}Ti_{40}$

3 Actuation Fatigue Life Prediction in SMAs in the Presence of Notches

The feasibility of SMAs is limited in many applications when considering only a smooth specimen. Notches are an important sector in the industry since they are prevalent in many different components and scales. They are, for example, present where bolt holes are needed and also at the microscopic level in the form of ‘micro-notches’. Under loading, these notches induce a stress concentration on the specimen, with a high stress level near the notch, leading to a lower lifetime; a reason why the lifetime results from smooth specimens cannot be utilized. As a result, a fatigue model that predicts the lifetime of SMA actuators in the presence of notches is required to increase usage in other areas and take advantage of what it offers.

3.1 Objective

The objective, as stated above, was to use the SWT model to predict the lifetime of notched specimens. To achieve this, the field intensity approach was taken. Ideally, a reasonable estimate of the lifetime should be achieved by choosing the point of maximum stress where the first cracks would appear. However, the lifetime determined by that method gives a highly conservative value. The field approach finds the average damage distribution over a critcal length to determine a more accurate lifetime [35]. Further, fatigue does not act on a single point but over a specific region [36]. By considering a region, the microcracks that are initiated within it is taken into account, which combine to form a macrocrack. This region can be either 1D or 2D which stretches over several grains allowing for a more accurate prediction.

3.1.1 Experiments

In [20], the individuals looked at plate actuator designs with a center hole (CH) and a single notch (N) composed of $Ni_{60}Ti_{40}$ (wt%). These plates have the dimensions of 100 mm long, 10 mm wide, and 0.5 mm thick and have received an identical heat treatment of 2 hours at 850^{o}C in an inert gas followed by 20 hours at 450^{o}C and water quenching. Each circular void has a radius of 1 mm and is located 1.03 mm away from the edge for the NH plates. A load of 86 and 118 MPa were added onto the N and CH plates respectively. Each test was repeated twice in the lab. The results obtained can be seen in Table 1 below.

Table 1: Experimental and Simulation Results

Specimen	*Test*	*Experimental Cycles to Failure*
Centered Hole	1	973
	2	872
Notched Hole	1	1523
	2	1573

By using the uniaxial experiments, the exponents a and b in the SWT equation, labeled as (2) above, is determined. This is crucial to do since the lifetime will be calculated using this equation and, therefore, having an accurate fit through the experimental data is necessary.

3.1.2 Simulations

To calibrate the SWT model, it has to be evaluated from numerical experiments in Abaqus. In Abaqus, a constitutive law is used to govern the parameters and take into account cyclic effects, like TRIP, which is explained in the appendix. The same specimens, center-hole and notched-hole, were used and constructed as shown in Figure 7. Due to symmetry, the specimen dimensions were revised to 50*10*0.5 mm.

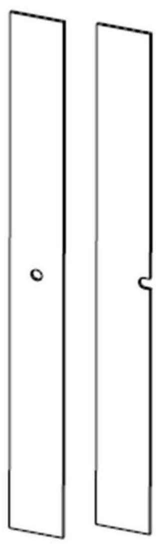

Figure 7: Actuator Plate Specimens

Since an SMA is a special material, the constitutive equations loaded in Abaqus cannot be used. In this case, a user-defined subroutine, called a UMAT, is utilized. A UMAT consists of equations from the constitutive model that govern the evolution of model parameters of transformation which consist of transformation hardening, stress required for transformation initiation and TRIP. The material properties are inputted in the order relative to how the UMAT code has been written. Table 2 shows the material properties.

Table 2: Parameter values corresponding to the $Ni_{60}Ti_{40}$ (wt%) material system tested.

(a) Elastic constants

parameter	value
E_A [MPa]	75150
ν_A	0.33
E_M [MPa]	51000
ν_M	0.33

(b) Transformation and plastic deformation constants

Phase transformation parameter values at the first and stable cycle:			
Initial set		Final set	
parameter	value	parameter	value
M^{0s} [K]	325.0	M^{0s} [K]	345.0
H^{max}	0.01296	H^{max}	0.001296
Y_0 [MJ/m^3]	4	Y_0 [MJ/m^3]	1.5
$\rho\Delta s_0$ [MJ/(m^{3}K)]	-0.38	$\rho\Delta s_0$ [MJ/(m^{3}K]	-0.25
D_1^d [MPa]	5	D_1^d [MPa]	12
D_2^d [MPa]	0.7	D_2^d [MPa]	0.5
		$\varepsilon^p_{sat} = C_1^p C_2^p$	0.014
Constants characterizing the evolution between the initial and stable values of the above parameters:			
λ_1	0.08		
λ_2	0.08		
C_2^p	12.4		
Constant characterizing maximum transformation strain as a function of stress			
k	0.0204		

100 steps are created, each representing one actuation cycle. The initial and maximum step sizes are kept at 0.001 since this gave both an accurate and stable solution. Next, the loads on the top surface and the x, y and z symmetry boundary conditions are added to the bottom surface. An amplitude is created to variate the temperature from 368 K to 184 K and then back to 368 K for each step. This temperature range

was large enough that it went below the martensitic finish temperature and above the austenitic start temperature. Figure 8 and 9 shows both specimen once all the loads and boundary conditions are applied.

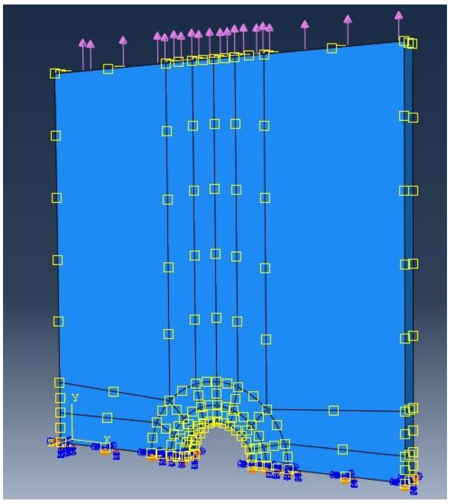

Figure 8: Loads and Boundary Conditions on Center Hole Specimen

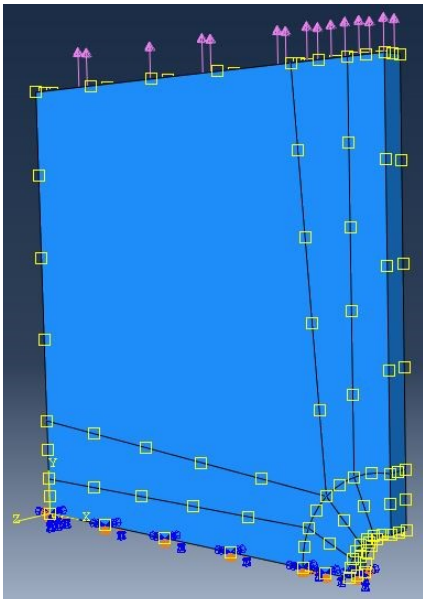

Figure 9: Loads and Boundary Conditions on Notched Hole Specimen

A fine, structured mesh made of linear, hexahedral elements of type C3D8 was created to get accurate results around the inclusion. A structured mesh was chosen to avoid sharp corners that may cause large element distortion and lead the simulation to terminate, while, linear elements was chosen since it leads to a faster computation. To achieve this, the specimen was partitioned and through local seeding the desired mesh was obtained. The mesh can be seen in Figure 10 and Figure 11 below.

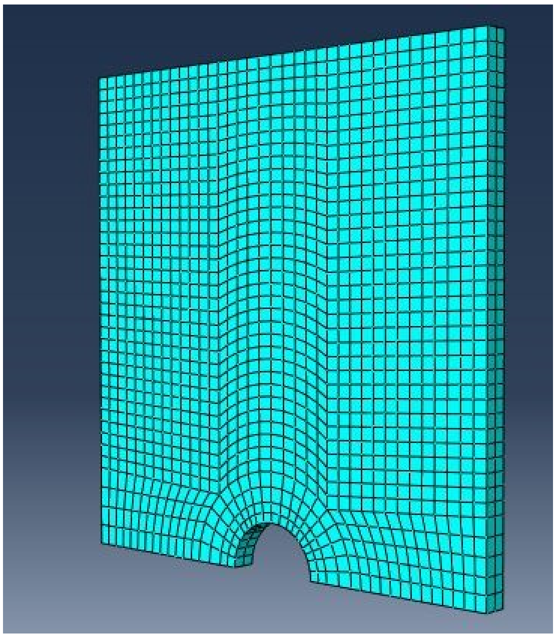

Figure 10: Mesh of Center - Hole Specimen

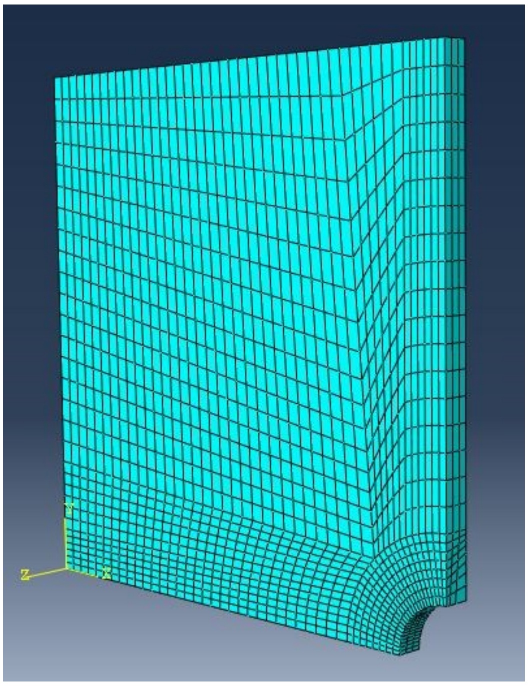

Figure 11: Mesh of Notched - Hole Specimen

The job is submitted and once completed, the temperature – strain graph is plotted to verify the results. A post-processing Python script is used to verify that the SWT parameter assumes greater values on the surface rather than within the material. Therefore, lines along the surface and on the plane of symmetry was chosen as the domain of integration for the SWT. A total of 7 material points were taken along the line. This was done for 20 consecutive cycles to calculate the SWT evolution for each material point. The evolution follows a logarithmic function in the form of $\lambda \log N + \mu$. Next, the evolution of λ and μ is determined to create an SWT equation as a function of r, the distance from the notch. This updated equation allows for the SWT intensity (SWT_I) to be calculated over a distance r in front of the notch root.

$$\mathrm{SWT}_I = \frac{1}{D} \int_D \mathrm{SWT}(\mathbf{r}) \varphi(\mathbf{r}) dD, \tag{3}$$

where $\mathrm{SWT}(\mathbf{r}) = \sigma_{max}(\mathbf{r})\varepsilon_\alpha(\mathbf{r})$ and $\varphi(\mathbf{r})$ is a weight function that depends on the position vector $\mathbf{r}$ from the notch root within the highly stressed volume domain D in which fatigue is expected. The weight function is introduced in order to capture notch geometry and size effects and it is dependent on loading type, boundary conditions, and material properties. Both originate primarily from stress gradients in an uneven field intensity while in an even field intensity the influence of size is mainly due to an increased number of fatigue damage sources in a larger specimen. $\varphi(\mathbf{r})$ should be equipped with the following properties [35]

- $0 \leq \varphi(\mathbf{r}) \leq 1$ is a decreasing function;
- $\varphi(\mathbf{0}) = 1$;
- $\varphi(\mathbf{r}) \equiv$ for $\nabla \sigma \equiv \mathbf{0}$, where σ is the stress tensor.

In this case, $\varphi(\mathbf{r}) = 1$ is one example of a weight function with the above properties. $\varphi(\mathbf{r}) = 1 - \left[1 - \frac{SWT(\mathbf{r})}{SWT_{max}}\right](1 + \sin\theta)r$ is the weight function proposed by [37], where r and θ are polar coordinates wth respect to the notch root axis.

The fatigue life is calculated by employing the Palmgren-Miner's linear damage rule [38], a cumulative damage model where fractional damage is integrated from 0 to N_f. The premise of this law is that the summation of the fractional damage shows the amount of lifetime the specimen has used.

$$\int_0^{N_f} \left[\frac{\mathrm{SWT}_I(N)}{a}\right]^{\frac{1}{b}} dN = \int_0^{N_f} \left[\frac{\frac{1}{r}\int_0^r \mathrm{SWT}(N)\varphi(r)dr}{a}\right]^{\frac{1}{b}} dN = 1, \tag{4}$$

where N_f is cycles to failure, r is the radius or critical length

The least-square fit method is utilized and run on Matlab to determine the parameters a, b, N, and r using each geometry, with a constraint that Miner's Law is satisfied. This equation was in the form of: $(experimental - predicted)^2$ where the experimental value is known and the predicted term was subtituted with equation (4), which represents the lifetime. The equation initially contains the smooth specimens from [20], in the form of a dogbone specimen, and center-hole. All four parameters are determined and the SWT is calculated for the center-hole specimen by substituting r and N into the equation. Next, the notched specimens are added into the least-square fit, and the lifetime of the notched specimen is acquired with the final SWT parameters, a and b. Finally, using the final SWT parameters a and b the predicted lifetimes of smooth specimens are found using the actuation work in [20]. The predicted lifetimes of all three specimens are compared to the experimental.

3.2 Results

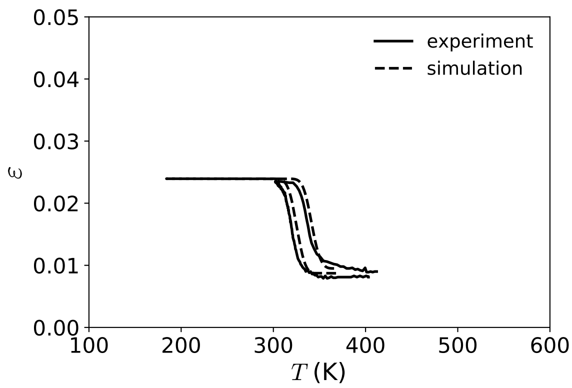

(a) 5^{th} cycle

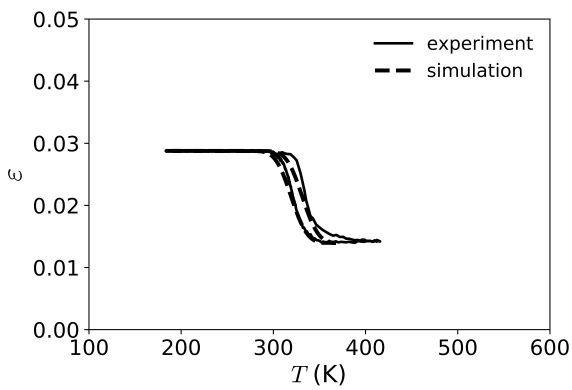

(b) 200^{th} cycle

Figure 12: Strain (in the direction of loading) vs temperature response of smooth specimen (D) during thermal cycling sweeps under constant uniaxial bias load of 300 MPa.

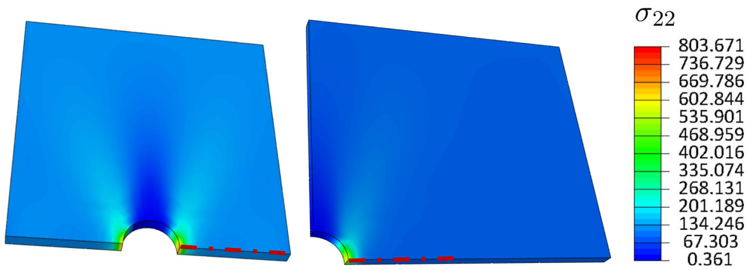

(a) 1^{st} cycle

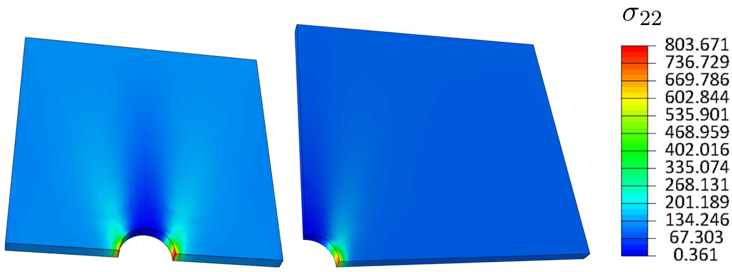

(b) 100^{th} cycle

Figure 13: Stress component, σ_{22}, *i.e.*, the component in the direction of loading at the end of cooling during the 1^{st} and $100th$ cycle for the (CH) and (N) geometries. The red dashed lines indicate the lines of integration of the SWT intensity, SWT_I. Note the increase in stress values at the $100th$ cycle as compared to the $1st$ cycle near the hole and notch for the (CH) and (N) geometries, respectively.

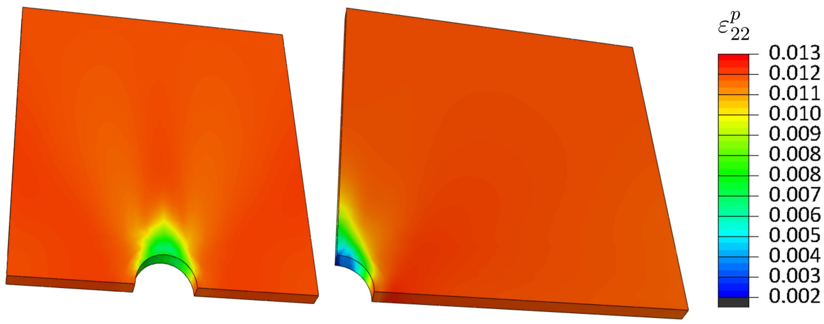

Figure 14: Plastic strain component, ε_{22}^{p} at the end of cooling during the $100th$ cycle for the (CH) and (N) geometries.

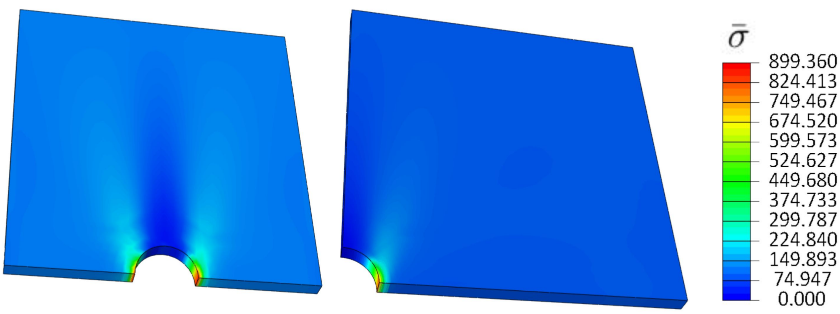

Figure 15: Von Mises stress at the end of cooling during during the $100th$ cycle for the (CH) and (N) geometries.

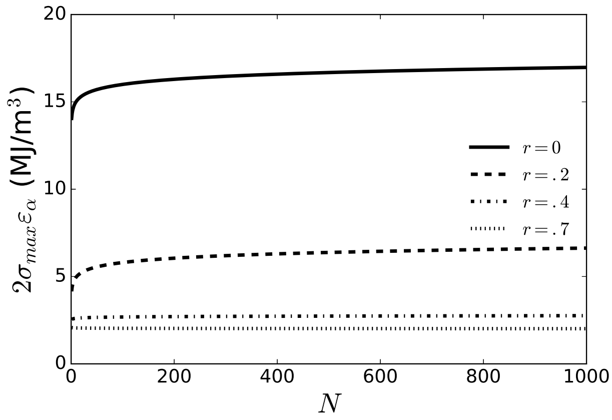

Figure 16: SWT parameter vs number of cycles at distances from the hole along the line of integration of SWT_I for CH specimens.

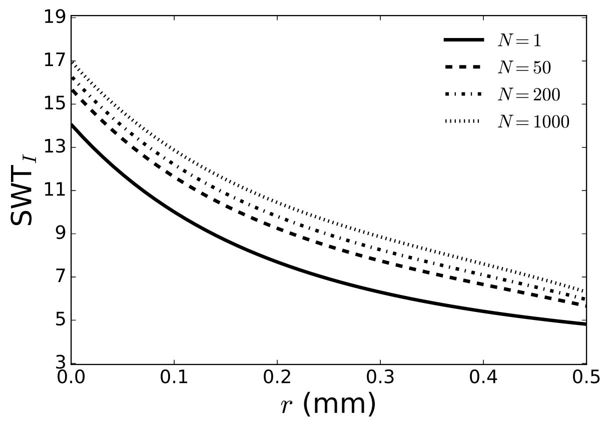

Figure 17: SWT_I vs distance from the hole along the line of integration at different number of cycles for CH specimens.

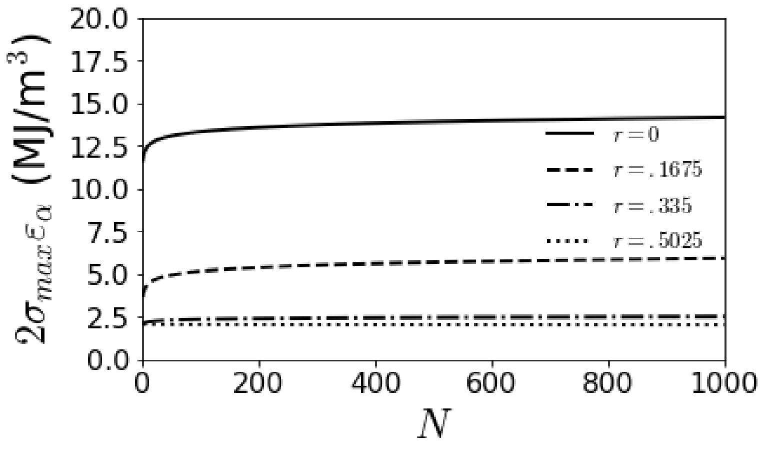

Figure 18: SWT parameter vs number of cycles at distances from the hole along the line of integration of SWT_I for N specimens.

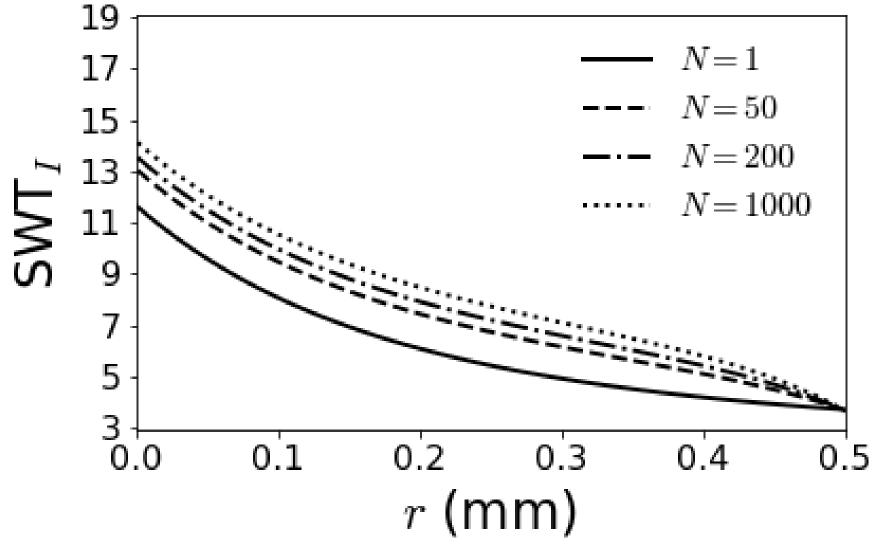

Figure 19: SWT_I vs distance from the hole along the line of integration at different number of cycles for N specimens.

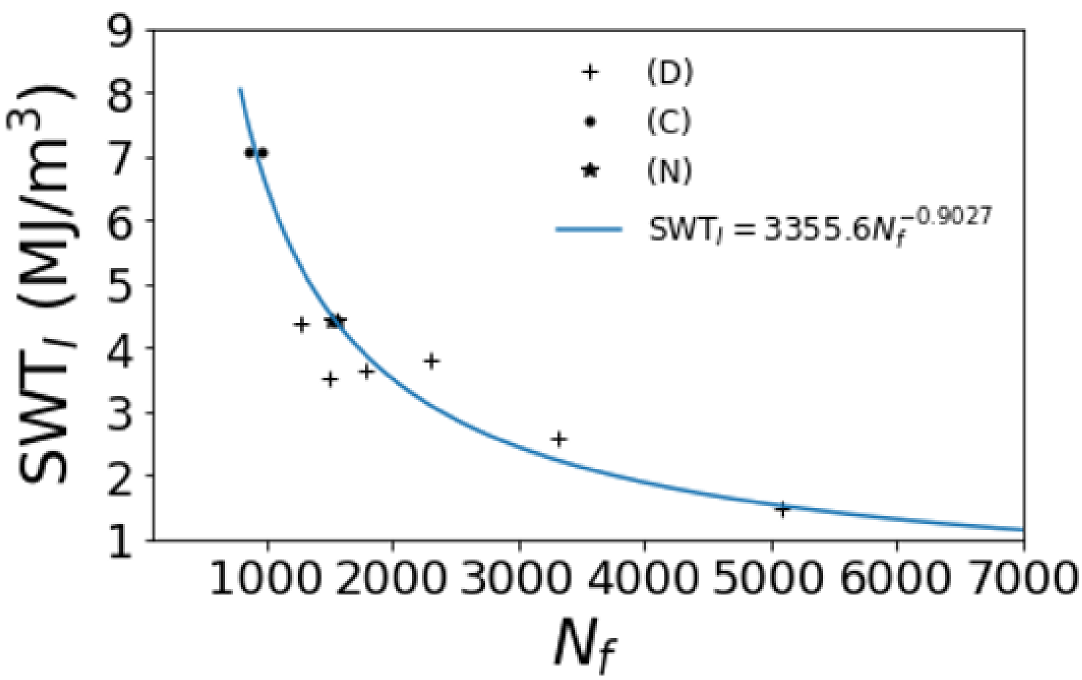

Figure 20: SWT_I vs lifetime for all experiments.

Table 3: Actuation Lifetime Prediction for (CH) and (N)

Specimen	Test	Experimental Lifetime	Predicted Lifetime	Critical length, r(mm)	a	b	SWT_I
Centered Hole	1	973	922	.4742	3355.6	.9027	7.0668
	2	872	922				
Notched Plate	1	1523	1548	.4742	3355.6	.9027	4.4288
	2	1573	1548				

Table 4: Actuation Lifetime Prediction for (DB)

Specimen	Load	Test	Experimental Lifetime	Predicted Lifetime
Dogbone	200	1	5080	5214
		2	3290	2817
Dogbone	250	1	2290	1815
		2	1790	1935
Dogbone	300	1	1490	2015
		2	1270	1567

3.3 Discussion

In Figure 12, uniaxial simulations are compared against experimental results. Simulations of the experiments performed are shown in Figures 13 and 14 where the stress distributions are shown at the end of cooling during the 1^{st} and 100^{th} cycle. As shown in Figure 13, the stress distribution at the 1^{st} cycle is different than that at the 100^{th} cycle due to accumulation of plastic strains that cause the redistibution. As mentioned before, phase transformation taking place during thermal cycling alters the stress values within each cycle and in the absence of plastic deformation, there would be no change in stresses from one cycle to another. The plastic strain component in the direction of loading is shown at the 100^{th} cycle in Figure 14. Further, both are dependent on load level and, therefore, assume larger values at the regions of greater von Mises stress values in Figure 15. The evolution of the SWT parameter with respect to the number of cycles can be seen in Figure 16 for the CH specimen at distances from the hole along the plane of symmetry. The SWT parameter evolves monotonically with cycling at distances close to the hole. Note that the SWT_I evolution with cycling depends solely on the accumulation of plastic strains which results in evolving stresses and strains values. The dependence of the SWT intensity on the distance r is shown in Figure 17. As expected SWT_I is a decreasing function of distance, whch explains why the conservative lifetime estimations based on the SWT parameter at the point of maximum damage, $r = 0$, can be altered if a domain is used instead. Figure 18, similarily to Figure 16, shows the evolution of the SWT parameter with respect to the number of cycles for the (N) specimen. The same trend of monotonic evolution is observed at distances close to the hole. Figure 19, shows the SWT intensity dependency on the distance r. It is seen to monotonically evolve for the first cycle, however, for the other cycles it is seen that they are converging near 0.5 mm. This can be due to the stress relaxation that occurs due to the high stresses near the notch. To accomodate the high stresses, the surrounding areas would reduce in stress, leading to a drop in the SWT parameter. Figure 20, lastly, shows the least-square fit of lifetimes vs SWT_I over all experiments to obtain the size of the domain of integration, r and constants a and b as explained above. The size of the domain of integration, $r = 0.48$ mm is considered representative of the size of the domain in which the micro-mechaniss of fatigue are most active, which, according to the experiments should span just a few grains. Table 3 shows the final results for the (CH) and (N) specimens containing the lifetime, critical length, average SWT parameter and the material properties, a and b. Table 4 shows the final results for (DB) specimens comparing the predicted and experimental lifetime.

4 Conclusions

The efficiency of the critical plane model of Smith, Watson, and Topper combined with the field intensity approach in estimating fatigue life for loaded notched shape memory alloys undergoing thermal cycling was demonstrated against experimental data on four different SMA actuator configurations. The field intensity approach, which characterizes the fatigue damage over the local region of damage rather at a point, is more reasonable from the point of view of fatigue failure mechanisms and more comprehensive from the point of view of explaining fatigue phenomena. The proposed method is limited to predicting crack initiation or final failure where the crack propagation stage is negligible. This is the case for the small notched specimens used to obtain the fatigue lifetime data. However, in service applications, crack propagation may occupy a widely varying portion of the useful life of notched members and structures. Weight critical structures that fail predominantly in a brittle manner, such as most envisioned SMA actuators, represent the extreme case in which crack propagation occupies a small fraction of the entire life.

References

[1] D. C. Lagoudas, *Shape memory alloys: modeling and engineering applications.* Springer Science & Business Media, 2008.

[2] K. Otsuka and C. Wayman, eds., *Shape Memory Materials.* Cambridge: Cambridge University Press, 1999.

[3] T. Duerig, K. Melton, D. Stockel, and C. Wayman, eds., *Engineering Aspects of Shape Memory Alloys.* London: Butterworth-Heinemann, 1990.

[4] S. Jape, T. Baxevanis, and D. Lagoudas, "On the fracture toughness and stable crack growth in shape memory alloy actuators in the presence of transformation-induced plasticity," *International Journal of Fracture*, vol. 209, no. 1-2, pp. 117–130, 2018.

[5] D. J. Hartl and D. C. Lagoudas, "Aerospace applications of shape memory alloys," Proceedings of the Institution of Mechanical Engineers, Part G: Journal of Aerospace Engineering, pp. 535–552, SAGE, 2007.

[6] M. Sreekumar, T. Nagarajan, M. Singaperumal, M. Zoppi, and R. Molfino, "Critical review of current trends in shape memory alloy actuators for intelligent robots," *Ind. Robot*, vol. 34, no. 4, pp. 285–294, 2007.

[7] D. J. Hartl and D. C. Lagoudas, "Aerospace applications of shape memory alloys," *Proceedings of the Institution of Mechanical Engineers, Part G: Journal of Aerospace Engineering*, vol. 221, no. 4, pp. 535–552, 2007.

[8] Y. C. Robert W Wheeler, Darren J Hartl, "Modeling of thermo-mechanical fatigue and damage in shape memory alloy axial actuators," 2015.

[9] C. Calhoun, *Actuation fatigue of shape memory alloys.* PhD thesis, Texas A & M University, 2012.

[10] S. Suresh, *Fatigue of Materials.* Cambridge University Press, 2 ed., 1998.

[11] J. Schubnell, V. Hardenacke, and M. Farajian, "Strain-based critical plane approach to predict the fatigue life of high frequency mechanical impact (hfmi)-treated welded joints depending on the material condition," vol. 61, 08 2017.

[12] J.-k. Zhang, X.-q. Cheng, and Z.-n. Li, "Total fatigue life prediction for ti-alloys airframe structure based on durability and damage-tolerant design concept," *Materials & Design*, vol. 31, no. 9, pp. 4329–4335, 2010.

[13] W. E. A. Paul C. Paris, Mario P. Gomez, "A rational analytic theory of fatigue," *The Trend in Engineering*, vol. 13, pp. 9–14, 1961.

[14] M. Bäckström and G. Marquis, "A review of multiaxial fatigue of weldments: experimental results, design code and critical plane approaches," *Fatigue & fracture of engineering materials & structures*, vol. 24, no. 5, pp. 279–291, 2001.

[15] M. de Freitas, L. Reis, M. A. Meggiolaro, and J. T. P. de Castro, "Comparison between ssf and critical-plane models to predict fatigue lives under multiaxial proportional load histories," *Frattura ed Integrità Strutturale*, vol. 10, no. 38, pp. 121–127, 2016.

[16] J. M. Jani, M. Leary, A. Subic, and M. A. Gibson, "A review of shape memory alloy research, applications and opportunities," *Materials & Design (1980-2015)*, vol. 56, pp. 1078–1113, 2014.

[17] P. S. Lobo, J. Almeida, and L. Guerreiro, "Shape memory alloys behaviour: A review," *Procedia Engineering*, vol. 114, pp. 776 – 783, 2015. ICSI 2015 The 1st International Conference on Structural Integrity Funchal, Madeira, Portugal 1st to 4th September, 2015.

[18] J. Perkins and R. Sponholz, "Stress-induced martensitic transformation cycling and two-way shape memory training in cu-zn-al alloys," *Metallurgical transactions A*, vol. 15, no. 2, pp. 313–321, 1984.

[19] E. Patoor, D. C. Lagoudas, P. B. Entchev, L. C. Brinson, and X. Gao, "Shape memory alloys, part i: General properties and modeling of single crystals," *Mechanics of materials*, vol. 38, no. 5-6, pp. 391–429, 2006.

[20] R. Wheeler, C. Ottmers, B. Hewling, and D. Lagoudas, "Actuator lifetime predictions for $Ni_{60}Ti_{40}$ shape memory alloy plate actuators," in *Behavior and Mechanics of Multifunctional Materials and Composites 2016*, p. 98000E, procspie, 2016.

[21] M. Thumann and E. Hornbogen, "Thermal and mechanical fatigue in Cu-based shape memory alloys," *Zeitschrift fuer Metallkunde/Materials Research and Advanced Techniques*, vol. 79, no. 2, pp. 119–126, 1988.

[22] G. Eggeler, E. Hornbogen, A. Yawny, A. Heckmann, and M. Wagner, "Structural and functional fatigue of NiTi shape memory alloys," *Mat. Sci. Eng. A-Struct.*, vol. 378, pp. 24–33, 2004.

[23] D. Achitei, D. Galuşca, P. Vizureanu, R. Carabet, and N. Cimpoeşu, "Aspects regarding thermo-mechanical fatigue of shape memory alloys," *Metal. Int.*, vol. 14, pp. 45–48, 2009.

[24] H. Meier, C. Haberland, and J. Frenzel, "Structural and functional properties of niti shape memory alloys produced by selective laser melting," in *Innovative Developments in Virtual and Physical Prototyping* (P. Bartolo, ed.), Conference on Advanced Research in Virtual and Rapid Prototyping, pp. 291–296, Taylor & Francis, 2012.

[25] D. König, R. Zarnetta, A. Savan, H. Brunken, and A. Ludwig, "Phase transformation, structural and functional fatigue properties of TiNiHf shape memory thin films," *Acta Mater.*, vol. 59, no. 8, pp. 3267–3275, 2011.

[26] C. Calhoun, R. Wheeler, T. Baxevanis, and D. Lagoudas, "Actuation fatigue life prediction of shape memory alloys under the constant-stress loading condition," *Scripta Materialia*, vol. 95, pp. 58–61, 2015.

[27] K. Smith, P. Watson, and T. Topper, "Stress–strain function for the fatigue of metals," *J Mater*, vol. 5, no. 4, pp. 767–778, 1970.

[28] M. Bigeon and M. Morin, "Thermomechanical study of the stress assisted two way memory effect fatigue in TiNi and CuZnAl wires," *Scripta Mater.*, vol. 35, no. 12, pp. 1373–1378, 1996.

[29] G. Scirè Mammano and E. Dragoni, "Effects of loading and constraining conditions on the thermomechanical fatigue life of NiTi shape memory wires," *J. Mater. Eng. Perform.*, vol. 23, no. 7, pp. 2403–2411, 2014.

[30] D. Lagoudas, D. Miller, L. Rong, and P. Kumar, "Thermomechanical fatigue of shape memory alloys," *Smart Mater. Struct.*, vol. 18, no. 8, p. 085021, 2009.

[31] O. Bertacchini, D. Lagoudas, and E. Patoor, "Thermomechanical transformation fatigue of TiNiCu SMA actuators under a corrosive environment — Part I: Experimental results," *Int. J. Fatigue*, vol. 31, no. 10, pp. 1571–1578, 2009.

[32] G. Ahmadzadeh and A. Varvani-Farahani, "Fatigue life assessment of steel samples under various multiaxial loading spectra by means of smith-watson-topper type damage descriptions," *Fatigue & Fracture of Engineering Materials & Structures*, 2018.

[33] K. Otsuka and X. Ren, "Recent developments in the research of shape memory alloys," *Intermetallics*, vol. 7, no. 5, pp. 511–528, 1999.

[34] A. Ince and G. Glinka, "A modification of morrow and smith–watson–topper mean stress correction models," *Fatigue & Fracture of Engineering Materials & Structures*, vol. 34, no. 11, pp. 854–867, 2011.

[35] Y. Weixing, "Stress field intensity approach for predicting fatigue life," *International Journal of Fatigue*, vol. 15, no. 3, pp. 243–246, 1993.

[36] S. Harvey, P. Marsh, and W. Gerberich, "Atomic force microscopy and modeling of fatigue crack initiation in metals," *Acta Metall. Mater.*, vol. 42, no. 10, pp. 3493–3502, 1994.

[37] "Local stress–strain field intensity approach to fatigue life prediction under random cyclic loading," *Int. J. Fatigue*, vol. 23, no. 10, pp. 903–910, 2001.

[38] H. Neuber, "Theory of stress concentration for shear-strained prismatical bodies with arbitrary nonlinear stress-strain law," *J. Appl. Mech., Transactions ASME*, vol. 28, no. 4, pp. 544–550, 1960.

[39] Z. Bo and D. C. Lagoudas, "Thermomechanical modeling of polycrystalline smas under cyclic loading, part i: theoretical derivations," *International Journal of Engineering Science*, vol. 37, no. 9, pp. 1089–1140, 1999.

[40] D. Lagoudas and Z. Bo, "Thermomechanical modeling of polycrystalline SMAs under cyclic loading, Part II: Material characterization and experimental results for a stable transformation cycle," *Int. Engng. Sci*, pp. 1141–1173, 1999.

[41] Z. Bo and D. Lagoudas, "Thermomechanical modeling of polycrystalline SMAs under cyclic loading, Part III: Evolution of plastic strains and two-way shape memory effect," *Int. Engng. Sci*, pp. 1175–1203, 1999.

[42] J. G. Boyd and D. C. Lagoudas, "A thermodynamical constitutive model for shape memory materials. Part I. The monolithic shape memory alloy," *Int. J. Plast.*, vol. 12, no. 6, pp. 805–842, 1996.

5 Appendix

5.1 Material Constitutive Model

The constitutive model is that proposed by Bo and Lagoudas [39, 40, 41], which is an extension of the constitutive model for polycrystalline SMAs undergoing solid-state diffusionless phase transformation developed by Boyd and Lagoudas [42].

Additive decomposition of the total strain tensor in an elastic, a transformation, and a plastic part is assumed and the classical, rate-independent, small-strain flow theory framework for the evolution of inelastic strains is adopted. Thus, the increments of the strain tensor components $d\varepsilon_{ij}$ are given as

$$d\varepsilon_{ij} = S_{ijkl} d\sigma_{kl} + dS_{ijkl}\sigma_{kl} + d\varepsilon^{t}_{ij} + d\varepsilon^{p}_{ij}, \tag{5}$$

where σ_{ij}, ε^{t}_{ij}, ε^{p}_{ij} are the Cartesian components of the stress tensor, transformation strain tensor, and plastic strain tensor, respectively, and S_{ijkl} are the components of the "current" compliance tensor. Throughout this paper, standard Einstein notation is used with summation over repeated indices assumed. The current compliance tensor varies with the martensitic volume fraction ξ as $S_{ijkl} = (1-\xi)S^{A}_{ijkl} + \xi S^{M}_{ijkl}$, where S^{A}_{ijkl} and S^{M}_{ijkl} are the components of the compliance tensor of austenite and martensite, respectively. In this paper, it is assumed that both austenite and martensite are isotropic and $S^{\alpha}_{ijkl} = \frac{1+\nu_\alpha}{2E_\alpha}(\delta_{il}\delta_{jk} + \delta_{ik}\delta_{jl}) - \frac{\nu_\alpha}{E_\alpha}\delta_{ij}\delta_{kl}$, where the index α stands for A in the case of austenite and for M in the case of martensite. E_α, ν_α denote the Young's modulus and Poisson's ratio, respectively, of the two phases and δ_{ij} is Kronecker's delta.

The plastic strain considered here is different from conventional plasticity in metals. Due to the misfit between the austenite–martensite interfaces, significant distortion is created. In addition, in a polycrystalline SMA, different grains transform in different manners, which causes additional distortion at the grain boundaries. These two phenomena act in concert, and the final result is an observable macroscopic plastic strain, which occurs at effective stress levels much lower than the plastic yield limit of the material without phase transformation. This model does not address the plastic strain evolution initiated when pure austenite or martensite is subjected to effective stresses that exceed the critical stress for slip, but is focused on plasticity caused by cyclic transformation only.

5.2 Evolution of transformation strains

An evolution equation of the transformation strain is defined so that it is related to the evolution of martensite volume fraction, ξ,

$$d\varepsilon_{ij}^t = \Lambda_{ij} d\xi, \quad \Lambda_{ij} = \begin{cases} \dfrac{3}{2} \dfrac{H^{cur}(\bar{\sigma})}{\bar{\sigma}} s_{ij}, & d\xi > 0, \\ \dfrac{\varepsilon_{ij}^t}{\xi}, & d\xi < 0, \end{cases} \tag{6}$$

where Λ_{ij} are the components of the direction tensor. Here, $H^{cur}(\bar{\sigma})$ is the uniaxial transformation strain magnitude for complete transformation, $\bar{\sigma} = \sqrt{\frac{3}{2} s_{ij} s_{ij}}$ is the Mises equivalent stress, and $s_{ij} = \sigma_{ij} - \sigma_{kk}\delta_{ij}/3$ are the stress deviator components. During forward transformation, the transformation strain is oriented by the direction of the deviatoric stress, which motivates the selected J_2 form of the direction tensor. During reverse phase transformation, it is assumed that the direction and magnitude of the transformation strain recovery is governed by the average orientation of the martensite at transformation reversal (the cessation of forward transformation, be it partial or full). This definition allows the transformation strain to return to zero for every state with a null martensite volume fraction.

$H^{cur}(\bar{\sigma})$ is a function of the stress state since most SMA materials do not exhibit a constant maximum attainable transformation strain at all stress levels. A saturated value of maximum attainable transformation strain, H^{max}, is reached at a high stress level, which is dependent on the SMA material as well as the processing conditions for a polycrystalline material, resulting in different crystallographic and morphological textures, for example. Following this observation, the maximum transformation strain $H^{cur}(\bar{\sigma})$ is represented by the following decaying exponential function

$$H^{cur}(\bar{\sigma}) = H^{max}\left(1 - e^{-k\bar{\sigma}}\right), \tag{7}$$

where the parameter k controls the rate at which $H^{cur}(\bar{\sigma})$ exponentially evolves from 0 to H^{max}. As the saturation value of the maximum transformation strain evolves with the number of cycles, its evolution is assumed to obey the following equation

$$H^{max} = (H)^{fin} + \left[(H)^{init} - (H)^{fin}\right] e^{-\lambda_1 \zeta^d}, \tag{8}$$

where $(H)^{fin}$ and $(H)^{init}$ are the final and initial values, and λ_1 is a positive material constant that governs the increasing rate of H^{max}.

5.3 Evolution of plastic strains

Similar to the evolution of transformation strain, the direction of plastic strain is determined by the direction of the applied stress. The development of the plastic strain is connected to the detwinned martensitic volume fraction, $\xi^d = \dfrac{H^{cur}(\bar{\sigma})}{H^{max}}\xi$, as

$$d\varepsilon_{ij}^p = \Lambda_{ij}^p d\xi, \quad \Lambda_{ij}^p = \begin{cases} \dfrac{3}{2} C_1^p \dfrac{H^{cur}(\bar{\sigma})}{H^{max}} \dfrac{s_{ij}}{\bar{\sigma}} e^{-\frac{\zeta^d}{C_2^p}}, & d\xi > 0 \\ \\ C_1^p \dfrac{H^{cur}(\bar{\sigma})}{H^{max}} \dfrac{\varepsilon_{ij}^t}{\xi} e^{-\frac{\zeta^d}{C_2^p}}, & d\xi < 0, \end{cases} \tag{9}$$

where Λ_{ij}^p are the components of the direction tensor,

$$\zeta^d = \int_0^t \frac{H^{cur}(\bar{\sigma})}{H^{max}} |\dot{\xi}| d\tau \tag{10}$$

is the accumulated detwinned martensite volume fraction. The material parameters C_1^p and C_2^p govern the saturation value of the plastic strain as well as the number of cycles necessary for its saturation.

5.4 Evolution of martensitic volume fraction

The evolution of the martensitic volume fraction can be inferred from the transformation surface

$$\Phi = 0, \quad \Phi = \begin{cases} \pi - Y, & d\xi > 0, \\ \\ -\pi - Y, & d\xi < 0, \end{cases} \tag{11}$$

where

$$\pi = \sigma_{ij}\Lambda_{ij} + \sigma_{ij}\Lambda_{ij}^p + \frac{1}{2}\Delta S_{ijkl}\sigma_{ij}\sigma_{kl} + \eta(\xi) + \rho\Delta s_0 \left(T - M^{0s}\right) + Y \tag{12}$$

In the above equation,

$$M^{0s} = T_0 + \frac{1}{\rho \Delta s_0} \left(Y + \rho \Delta u_0 \right) \tag{13}$$

is the initial martensitic-start temperature, s_0 and u_0 are the specific entropy and internal energy, respectively, ρ is the density, Δ denotes the difference in property between the martensitic and the austenitic states, Y is a material constant representing a measure of the internal dissipation during phase transformation, and

$$\eta = -D_1^d \left[-\ln(1-\xi) \right]^{\frac{1}{m_1}} + D_2^d \xi \tag{14}$$

is the drag stress that accounts for the isotropic hardening. The latter coefficients are assumed to change with the evolution of the accumulated detwinned martensitic volume fraction ζ^d as

$$D_i^d = \left(D_i^d \right)^{fin} + \left[\left(D_i^d \right)^{init} - \left(D_i^d \right)^{fin} \right] e^{-\lambda_2 \zeta^d}, \tag{15}$$

where $\left(D_i^d \right)^{fin}$ and $\left(D_i^d \right)^{init}$ are the final and initial values of the parameter, and λ_2 is a positive material constant governing the evolution of D_i^d. The equations governing the change of Y, M^{0s}, and $\rho \Delta s_0$ are assumed similar to (15)

$$Y = (Y)^{fin} + \left[(Y)^{init} - (Y)^{fin} \right] e^{-\lambda_2 \zeta^d}, \tag{16}$$

$$M^{0s} = \left(M^{0s} \right)^{fin} + \left[\left(M^{0s} \right)^{init} - \left(M^{0s} \right)^{fin} \right] e^{-\lambda_2 \zeta^d}, \text{ and} \tag{17}$$

$$\rho \Delta s_0 = (\rho \Delta s_0)^{fin} + \left[(\rho \Delta s_0)^{init} - (\rho \Delta s_0)^{fin} \right] e^{-\lambda_2 \zeta^d} \tag{18}$$

Constraints on the evolution of ξ are expressed in terms of the Kuhn-Tucker conditions given for forward and reverse phase transformation as

$$d\xi \geq 0, \quad \Phi \leq 0, \quad \Phi d\xi = 0 \text{ and} \tag{19}$$

$$d\xi \leq 0, \quad \Phi \leq 0, \quad \Phi d\xi = 0 \tag{20}$$

5.5 Model calibration

Two sets of the material parameters need to be identified from uniaxial experiments: the initial set, characterizing the initial response of the annealed material (denoted by the superscript ^{init}), and the final set, characterizing the stable material response (denoted by the superscript ^{fin}. The elastic stiffness E_A is determined by calculating the initial slope of the stress–strain curve for a uniaxial superelastic test. The elastic stiffness of the martensite phase E_M is given by the slope of the stress-strain curve at the point of initial unloading. The Poisson's ratios of austenite and martensite are assumed equal, with a typical reported value of $\nu_A = \nu_M = 0.33$. The martensitic start temperature, M_s, can be obtained from a DSC test. The maximum transformation strain, H^{max}, is obtained by extending the initial unloading part of the stress–strain curve of a superelastic experiment using the elastic stiffness of the martensitic phase, E_M until it meets the abscissa. The value of Y is related to the total area A enclosed by the hysteresis curve during a complete phase transformation as $A = 2Y$. $\rho\Delta s_0$ is given as $\rho\Delta s_0 = -\left[0.5\left(\sigma^{M_s}\right)^2 \Delta S + \sigma^{M_s} H^{cur}\left(\sigma^{M_s}\right)\right) / \left(T - M^{0s}\right]$, where σ^{M_s} represents the required stress level for initiation of phase transformation of the virgin material at a given temperature T. The K parameter is fitted by isobaric experimental results on the attainable transformation strain upon full transformation at different bias load levels. The drag stress parameters D_1^d and D_2^d and the exponent m_1 can be calibrated by least-square fitting of the experimental tangent stiffness during transformation to the tangent stiffness expression derived by the model. The parameters C_1^p and C_2^p are related to the saturated value of the plastic strain, $C_1^p C_2^p = \varepsilon_{sat}^p$. C_2^p can be approximated by enforcing the plastic strain $\varepsilon^p = \varepsilon_{sat}^p\left[1 - \exp(2N/C_2^p)\right]$ to approach the maximum value ε^p after the required number of cycles $N = N_{sat}^p$. The parameter $\lambda_1 = \lambda_2$ can be determined in a similar fashion so that the various parameters assume their final values after $N = N_{sat}^{b\,(\mathrm{or}\,d)}$ cycles. For further details, the reader is referred to [39, 40, 41].